Defects in nanosilica catalytically convert CO_2 to methane without any metal and ligand

Amit K. Mishra[a], Rajesh Belgamwar[a], Rajkumar Jana[b], Ayan Datta[b], and Vivek Polshettiwar[a,1]

[a]Department of Chemical Sciences, Tata Institute of Fundamental Research, Mumbai 400005, India; and [b]School of Chemical Sciences, Indian Association for the Cultivation of Science, Kolkata 700032, India

Edited by Alexis T. Bell, University of California, Berkeley, CA, and approved February 18, 2020 (received for review October 3, 2019)

Active and stable metal-free heterogeneous catalysts for CO_2 fixation are required to reduce the current high level of carbon dioxide in the atmosphere, which is driving climate change. In this work, we show that defects in nanosilica (E′ centers, oxygen vacancies, and nonbridging oxygen hole centers) convert CO_2 to methane with excellent productivity and selectivity. Neither metal nor complex organic ligands were required, and the defect alone acted as catalytic sites for carbon dioxide activation and hydrogen dissociation and their cooperative action converted CO_2 to methane. Unlike metal catalysts, which become deactivated with time, the defect-containing nanosilica showed significantly better stability. Notably, the catalyst can be regenerated by simple heating in the air without the need for hydrogen gas. Surprisingly, the catalytic activity for methane production increased significantly after every regeneration cycle, reaching more than double the methane production rate after eight regeneration cycles. This activated catalyst remained stable for more than 200 h. Detailed understanding of the role of the various defect sites in terms of their concentrations and proximities as well as their cooperativity in activating CO_2 and dissociating hydrogen to produce methane was achieved.

CO_2 | methane | defects | nanosilica | climate change

An excessive amount of carbon dioxide is the main cause of climate change. One of the best approaches is to capture and convert carbon dioxide (CO_2) into a green fuel such as methane (1–3). On the other hand, a sustainable way to solve the energy problem is to generate alternative energy source, however, challenges related to the storage of renewable electricity prevent the development of these technologies. Thus, CO_2 conversion to methane using renewable hydrogen has great potential and can provide a solution to these two problems of excessive CO_2 levels, and the temporal mismatch between renewable electricity production and demand as well as hydrogen storage (1–3).

The CO_2 methanation process needed metal-based catalysts (1–4). CO_2 hydrogenation was also achieved by metal/metal oxide hybrids and metal hydrides (1, 5–12). CO_2 polymerization was although reported by metal-free catalysts (13). The critical challenge for the reported metal catalysts is the poor stability due to oxidation and/or sintering of active sites (metal nanoparticles), as methanations are high-temperature reactions. Several attempts have been made to make them stable but because of the high surface energy of metal nanoparticles, they tend to oxidize or sinter/agglomerate on exposure to heat and/or air.

Thus, there is an urgent need to discover and develop a heterogeneous catalyst which is highly active, selective, and stable. It is well-known that the presence of various defects in nanomaterials endows them with a variety of functions (2, 8, 14–18). However, the ability to control and tune the type, concentration, and distribution of the various defects on the surface of nanomaterials is a considerable challenge.

In this work, we have developed the magnesiothermic defect engineering protocol to design a catalyst system where metal nanoparticle active sites were replaced with defects as catalytically active sites. We generated and tuned the defects (type, concentration, and proximity) in the nanosilica which were capable of catalytically converting CO_2 to methane with excellent productivity, selectivity, and stability. Neither metal nor complex organic ligands were used in this protocol.

Results and Discussion

In amorphous silica, defects are sites where the ideal Si and O network is broken (14–17). Amorphous silica contains three main defect sites: oxygen-deficient centers (ODC), E′-centers (≡Si•), and nonbridging oxygen hole centers (NBOHCs, ≡Si–O•) (*SI Appendix*, Fig. S1) (18–22). We used our patented high-surface-area dendritic fibrous nanosilica (DFNS) to generate large concentrations of surface defects, due to its unique fibrous morphology and good thermal stability (23, 24). Our first step was to develop a synthetic protocol to produce defects of the desired type, optimized concentration, and their distribution and proximities on the surface of the nanosilica. We achieved this by using a postsynthetic magnesiothermic protocol (25, 26). In principle, two moles of gaseous magnesium (Mg) react with one mole of silica to yield pure silicon at 650 °C (26). We optimized this reaction in such a way that reaction proceeded only partly, producing defect-containing silica. To tune the defects, DFNS was heated with varying concentrations of Mg at 675 °C for 12 h in a sealed quartz tube, which was evacuated at 120 °C overnight before sealing, for the oxygen-free environment. The tube was then cooled and broken to recover the products, defect-containing nanosilica, and magnesium species (Mg, MgO, and Mg_2Si). The Mg species was then removed by repeated washing with dilute hydrochloric acid in a water–ethanol mixture. The obtained

Significance

Reducing the CO_2 levels in Earth's atmosphere is key to stop further environmental degradation. CO_2 conversion to methane (green fuel) using renewable hydrogen is considered as one of the best options with great potential for simultaneously resolving energy and environmental challenges, although the production of hydrogen from renewable resources also needs to be economically viable. Unfortunately, this process needs an expensive metal or complex organometallics and most of them suffer from instability and poor selectivity toward methane. In this work, using the defect engineering approach, we develop metal-free–ligand-free nanocatalysts, which convert CO_2 to methane at the significant rates, scales, and stabilities.

Author contributions: V.P. designed the research project; A.K.M., R.B., and V.P. performed research (synthesis, characterization, and catalysis); A.K.M., R.B., and V.P. analyzed data; R.J. and A.D. performed computational study; and A.K.M. and V.P. wrote the paper.

The authors declare no competing interest.

This article is a PNAS Direct Submission.

[1]To whom correspondence may be addressed. Email: vivekpol@tifr.res.in.

This article contains supporting information online at https://www.pnas.org/lookup/suppl/doi:10.1073/pnas.1917237117/-/DCSupplemental.

First published March 10, 2020.

defect-containing nanosilica was denoted as DNS-X, where X indicates the amount of Mg (wt % with respect to nanosilica) used during the magnesiothermic protocol, 10, 25, and 50 wt % (Fig. 1).

The fibrous morphology of DFNS remains intact after the magnesiothermic treatment (Fig. 1), but with a systematic loss in textural properties with increase in Mg wt %. The nitrogen sorption isotherms (Fig. 1, *a3–d3*) showed typical type-IV curves with hysteresis. The Brunauer–Emmett–Teller (BET) surface area (S.A.) decreased from the original 537 m^2 g^{-1} for DFNS to 470, 396, and 100 m^2 g^{-1} for DNS-10, -25, and -50, respectively, due to the loss of its fibrous morphology with increasing amount of magnesium. The powder X-ray diffraction (PXRD) (*SI Appendix*, Fig. S2) and selective area electron diffraction (SAED, *SI Appendix*, Fig. S2) indicated that defect-containing silica is still amorphous in nature with some silicon impurities. Ultraviolet-visible diffuse reflectance (UV-DRS) spectra of the defect-containing nanosilica showed the weak absorption bands assigned to various defect sites (*SI Appendix*, Fig. S3).

The light emitters in silica are known to be NBOHCs, hydrogen-related species (≡Si-H), dioxasilirane, and silylene moieties (22, 27, 28). In qualitative analysis, the as-prepared defect-containing silica appears white, becoming gray with increasing defect concentration (*SI Appendix*, Fig. S4). When the samples were illuminated with UV lamp, very strong luminescence was observed, with colors changing from red to brown with increasing defect concentration from DNS-10 to DNS-50, indicating the variation in concentration and types of defect sites in these samples (*SI Appendix*, Fig. S4). In quantitative photoluminescence (PL) studies using a 374-nm excitation laser, the PL spectra of all samples contain two major broad peaks at 430 and 810 nm (Fig. 2 *A* and *B*). The peak at 430 nm was assigned to the dioxasilirane and silylene moieties (22), with highest intensity in DFNS. The broad PL band in the range of 600–1,030 nm with a peak maxima at 810 nm was assigned to NBOHC sites (29). The broadness of the PL signals was caused by the heterogeneity in the surrounding environment of the NBOHCs given the amorphous nature of the silica network. The intensities of the bands at 600–1,030 nm arising from NBOHC sites increased from DFNS to DNS-10 and then decreased in DNS-25 with no emissive peak in DNS-50 (Fig. 2*B*). This indicates that the magnesiothermic treatment generated more NBOHC sites in DNS-10. However, with increasing magnesium concentration, the intensity of this signal decreased significantly from DNS-10 to DNS-25, because of the conversion of NBOHC sites to E′ centers via the removal of oxygen from the NBOHC sites. As the magnesium concentration increased, further oxygen removal from NBOHC took place, and most of the NBOHC sites were converted into E′ centers; hence, no emission was observed in DNS-50 (Fig. 2*B*).

In the electron paramagnetic resonance (EPR) analysis, the peaks at g = 2.005, 2.0078, and 2.0094 were assigned to the E′ centers (30), peroxy centers (27), and NBOHCs (27) sites, respectively (*SI Appendix*, Fig. S5, *Left*). The EPR spectra of DFNS suggest that it does not contain paramagnetic centers (or their concentrations were negligible) whereas that of DNS-10 contain two peaks at 2.005 and 2.0094, corresponding to E′ centers and NBOHCs, respectively. The EPR spectrum of DNS-25 contains a peak at g = 2.0078, which corresponds to peroxy centers,

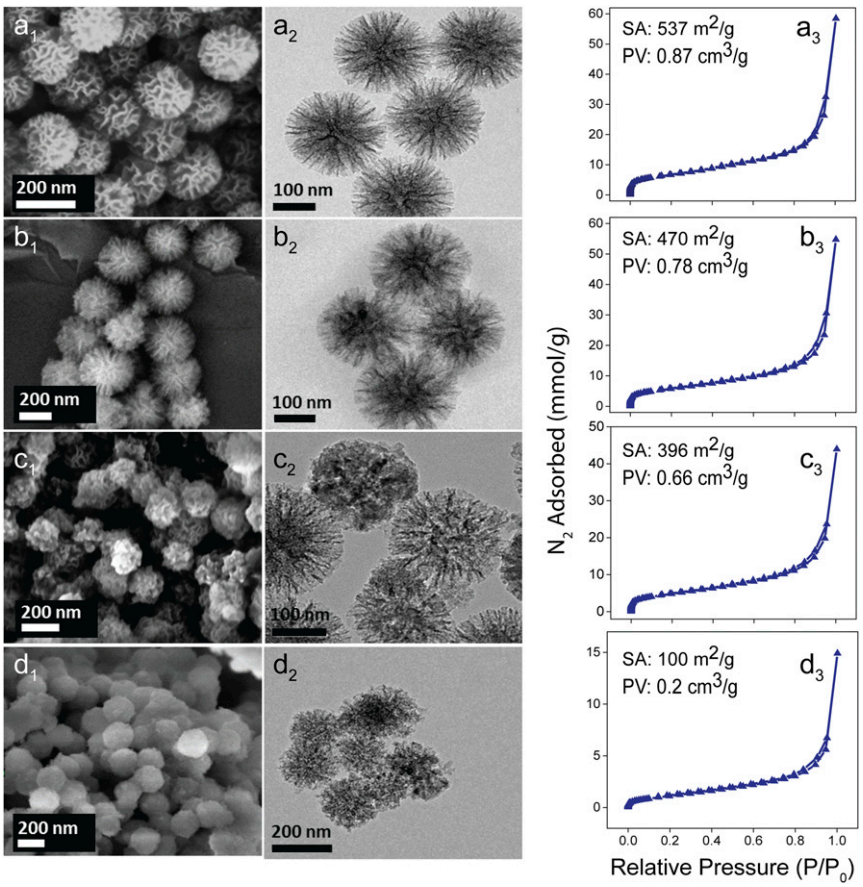

Fig. 1. Scanning electron microscopy (A_1–D_1), TEM (A_2–D_2), and N_2 sorption data (A_3–D_3). Surface area (SA) and pore volumes (PV) of (*A*) DFNS, (*B*) DNS-10, (*C*) DNS-25, and (*D*) DNS-50 are shown in upper left of A_3–D_3.

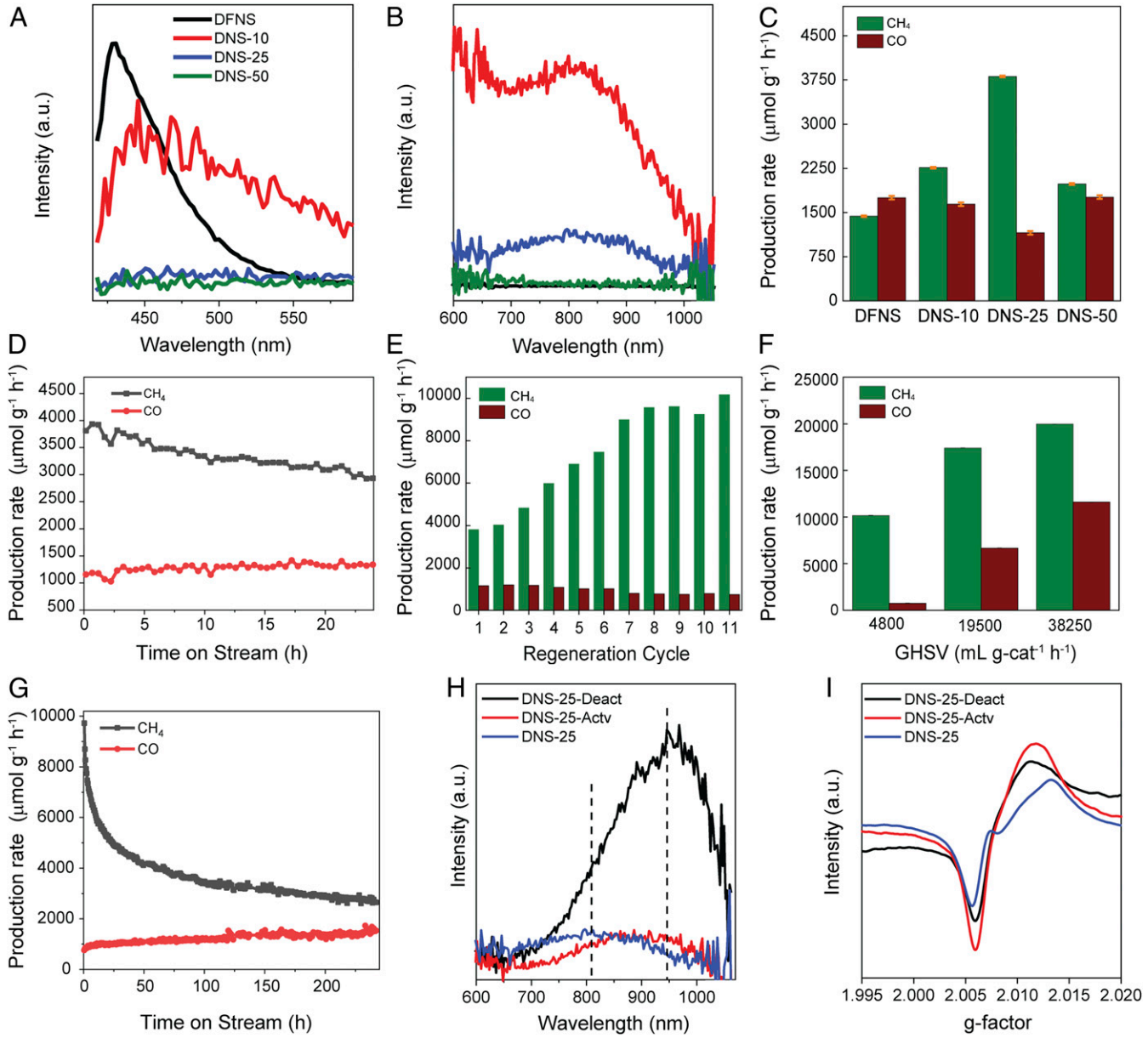

Fig. 2. (*A* and *B*) Photoluminescence emission spectra with an excitation wavelength (λ_{exc})= 374 nm. (*C*) Production rates of CH_4 and CO for various catalysts at 400 °C and 1 bar. (*D*) Stability test of DNS-25 at 400 °C and 1 bar. (*E*) Regeneration of catalysts in air at 400 °C and 1 bar for 11 cycles. (*F*) Production rate of CH_4 and CO with the activated DNS-25 at various GHSVs. (*G*) Stability test of activated DNS-25 at 400 °C and 1 bar for 200 h. (*H*) PL and (*I*) EPR, spectra of as-prepared DNS-25, activated DNS-25-Actv, and deactivated DNS-25-Deact.

whereas the peak at 2.0094 for NBOHCs was not clear because of the distortion in the peak of E′ centers. The EPR spectrum of DNS-50 contains two peaks at g = 2.005 and 2.0078, corresponding to the E′ centers and proxy centers, respectively, while no peak corresponding to the NBOHC centers was observed. The intensity of the peak at g = 2.005 (for E′ centers) increased continuously with an increasing amount of magnesium from DNS-10 to DNS-50, indicating the continuous increase of E′ centers concentration from DNS-10 to DNS-50.

To explore the types and concentrations of defects further, X-ray photoelectron spectroscopy (XPS) (*SI Appendix*, Fig. S5, *Right*) and Auger spectroscopy (*SI Appendix*, Fig. S6) studies were conducted. The XPS spectra of all samples contained four peaks for O (1s) at binding energies (BE) of 527.8, 529.7, 531.5, and 532.8 eV. The peak at 532.8 eV was assigned to the characteristic peak for oxygen arising from the siloxane framework of silica (31), whereas the peak at ~531.5 eV was attributed to silanol groups (32). The peak at 529.7 eV corresponds to NBOHC sites and the peak at 527.8 eV corresponds to peroxy radical. The Si (2p) spectra of all samples contain peaks at BEs of 103.8, 102, and 100.6, which were assigned to the characteristic peaks of Si in the siloxane framework, silanol, and NBOHCs, respectively. The origin of the peak at 99.1 eV is still not clear, but it may be ascribed to elemental silicon or peroxy radical as it follows the percentage area trend of the O (1s) of the peroxy radicals (*SI Appendix*, Table S1).

Conversion of CO_2 to Methane Catalyzed by Defect-Containing Nanosilica. The catalytic activity of defect-containing nanosilica for CO_2 methanation was studied using a fixed-bed microactivity reactor under flow conditions (*SI Appendix*, Fig. S7). We first evaluated the defect-containing silica for CO_2 methanation at

400 °C temperature and 1 bar pressure (Fig. 2*C* and *SI Appendix*, Fig. S8 for the progress of the catalytic reaction with time). The methane production rate increased from 1,436 μmol $g^{-1}{\cdot}h^{-1}$ for DFNS to 2,261 μmol $g^{-1}{\cdot}h^{-1}$ for DNS-10. DNS-25 showed the highest production rate of 3,810 μmol $g^{-1}{\cdot}h^{-1}$. For DNS-50, the methane production rate was only 1,983 μmol $g^{-1}{\cdot}h^{-1}$. Thus, the activity trend was DNS-25 > DNS-10 > DNS-50 > DFNS (Fig. 2*C*). The CO production rate was around 1,700 μmol $g^{-1}{\cdot}h^{-1}$ for most of the defect-containing nanosilica, while lowest CO formation was obtained for DNS-25 (1155 μmol $g^{-1}{\cdot}h^{-1}$). Even at a high pressure of 10 bar, DNS-25 showed the best activity for methane production of 4,995 μmol $g^{-1}{\cdot}h^{-1}$ (*SI Appendix*, Fig. S9).

We then studied the catalyst stability of the best catalyst (DNS-25) over 24 h and results indicated that the catalyst possesses good stability (Fig. 2*D*). The moderate decrease in activity and selectivity could be either due to carbon decomposition on the active sites or due to conversion of the defect sites into other types of defects during catalysis. The possibility of carbon decomposition was ruled out by Raman measurements of the spent catalysts (*SI Appendix*, Fig. S10), and temperature-programmed oxidation in thermogravimetric analysis (TGA) (*SI Appendix*, Fig. S11), which showed no sign of carbon. Carbon balance calculations (*SI Appendix*, *Experimental*) and no CO_2 detection during desorption from 400 to 550 °C also confirmed no carbon formation.

Notably, we were able to regenerate the catalysts by simply heating them in the air at 550 °C (Fig. 2*E*). On the regeneration of the catalyst (DNS-25) after every 24-h reaction cycle, we found that the catalytic activity increased significantly, after every regeneration cycle. The catalytic activity then became saturated after eight regeneration cycles where the methane production rate (9,569 μmol $g^{-1}{\cdot}h^{-1}$) was more than double that of the initial production rate (3,810 μmol $g^{-1}{\cdot}h^{-1}$). Like DNS-25, DNS-10 and even DFNS showed an increase in methane yield after every regeneration cycle (*SI Appendix*, Figs. S12 and S13).

Using this activated DNS-25 catalyst, we studied the effect of temperature on CO_2 methanation (*SI Appendix*, Fig. S14). The reaction temperature of 400 °C and a pressure of 1 bar were the optimal conditions for CO_2 methanation, and the subsequent studies were conducted using these reaction conditions. We then monitored the catalytic reactions at various gas hourly space velocity (GHSV) values and found that methane and CO production increases with an increase in GHSV (Fig. 2*F*).

Notably, when we conducted another stability study using the activated DNS-25 catalyst (Fig. 2*G*), after an initial decrease in catalytic activity, methane yield was stabilized at ∼3,000 μmol $g^{-1}{\cdot}h^{-1}$ and remained stable for more than 200 h.

One of the most critical aspects of this work was whether it is Mg or Mg species, which may be present in small concentrations even after washing, that catalyze the reaction rather than defect sites. We conducted a detailed analysis to study this aspect. From comparison with reported PXRD patterns of various Mg species (*SI Appendix*, Fig. S15), we observed that washed samples did not contain either Mg, MgO, or Mg_2Si. XPS analysis also indicated the absence of any Mg species (*SI Appendix*, Fig. S16). Energy-dispersive X-ray spectroscopy (EDS) elemental analysis in transmission electron microscope (TEM) indicated the presence of a small percentage of Mg in the case of DNS-10 (0.064 wt %) and DNS-50 (0.06 wt %) (*SI Appendix*, Figs. S17–S19), while no Mg was present in DNS-25. Pure nanosilica and DNS-25 which have no magnesium showed good catalytic activity for CO_2 methanation, ruling out the catalytic role of Mg species. To further confirm that small traces of Mg are not participating in catalysis, we have then carried out catalysis with unwashed and partially washed silicas having a known amount of Mg contents in defect-containing silica (*SI Appendix*, Fig. S20). We observed low catalytic activity (1,510 μmol $g^{-1}{\cdot}h^{-1}$ of methane) of the unwashed sample (DNS-25 with 21 wt % Mg), as the defect sites were covered by various Mg species. For a partially washed sample (DNS-25 with 4 wt % Mg), catalytic activity was 3,757 μmol $g^{-1}{\cdot}h^{-1}$ of methane, similar to pure defect-containing silica (DNS-25 with no Mg), 3,810 μmol $g^{-1}{\cdot}h^{-1}$. These experiments further confirm no role of Mg in the CO_2 methanation reaction. Another possibility of active sites is metal contamination in the reactor tube. We, therefore, carried out the catalysis using brand new reactor tubes made of stainless steel as well as Hastelloy C. In both cases, catalytic results were reproducible within the error bar confirming the defect sites are catalyzing the reactions. However, pure DFNS (before defect creation) also showed catalytic activity (Fig. 2*C*), which has a very low concentration of E′ and NBOHC defect sites. This indicates some role of walls of the reactor tube and/or frit in activating these defect sites, which need further investigation.

Cooperativity of Defect Sites. The results of PL, EPR, and XPS studies showed that DNS-10 has the highest amount of NBOHC sites, whereas DNS-50 has the highest number of E′ centers. However, the highest catalytic activity was shown by DNS-25. This suggests that CO_2 methanation requires an optimized concentration of these defect sites, and they work synergistically to convert CO_2 to methane. This hypothesis was able to explain why the catalytic activity increased with each regeneration cycle. We carried out PL and EPR analysis of the DNS-25 at three different stages of the reaction (Fig. 2 *H* and *I*); the as-prepared catalyst (DNS-25), the highly activated catalyst after 11 cycles (DNS-25-Actv), and the deactivated catalyst (DNS-25-Deact). The PL spectrum of the as-prepared DNS-25 contains a broad emission peak at 810 nm (Fig. 2*H*). The activated (DNS-25-Actv) catalyst showed an intense broad peak at 950 nm, as well as at 810 nm. It is known that the emission of bulk NBOHCs occurs at a lower wavelength than the emission of surface NBOHCs (27). Hence, the emission at 810 nm was assigned to the bulk NBOHCs whereas the strong emission at 950 nm was assigned to the surface NBOHCs. Increased peak intensity in deactivated catalyst at 950 nm suggests the generation of more surface NBOHCs sites during the catalysis (Fig. 2*H*).

The EPR spectrum of the as-prepared catalyst contains two peaks at g = 2.005 and 2.0078 arising from the E′ centers and peroxy centers, respectively (Fig. 2*I*). The disappearance of the peak at g = 2.0078 in the activated catalyst (DNS-25-Actv) indicated the loss of peroxy defect centers after regeneration. The increase in the peak intensity at g = 2.005 for the activated catalyst indicated the generation of more E′ centers. On the other hand, in the deactivated catalyst, the intensity of the peak corresponding to the E′ centers decreased while the intensity of surface NBOHCs sites increased (Fig. 2*I*). The E′ centers increased after air treatment and while NBOHCs increased during catalysis. Thus, with each regeneration cycle, the concentration of both the defects sites increased and hence the increase in catalytic activity was observed after every regeneration. The EPR, and PL analysis of catalyst at various intermediate cycles also confirms the systematic increase in these defect sites (*SI Appendix*, Figs. S21 and S22).

During stability studies, although methane formation rate decreased, the CO formation rate was not affected (Fig. 2*D*). This indicated that the defect sites that are disassociating H_2 (a key step for methane formation) must be also decreasing during catalysis. As E′-centers concentration decreased during the reaction, they must be responsible for the H_2 dissociation during catalysis. The increase in the formation rate of CH_4 after each regeneration cycle is due to the formation of more E′ centers during regeneration as well as more NBOHC sites formed during catalysis. This, in turn, increased the proximity of these defect sites, and they cooperatively converted CO_2 to methane. Although we are not certain about the pathway of formation of NBOHC centers during

catalysis, it could be due to the possible conversion of CO_2 adsorbed on E′ center into CO and NBOHC.

Proposed Mechanism of CO_2 Conversion by Defects. To obtain mechanistic insights into CO_2 conversion, we carried out diffuse reflectance infrared Fourier transform (DRIFT) spectroscopy measurements of the DNS-25 catalyst, under catalytic conditions (*SI Appendix*, Fig. S23) (33–40). The appearance of signals at 3,658–3,625, and 3,600 cm^{-1} can be attributed to the strong interactions of CO_2 with the silanols, generating bicarbonate and silanols with different environments (33, 40). The peak at 810 cm^{-1} represents the bending of Si–O bond, and the broadness of this peak suggests the presence of defects such as NBOHC and peroxy centers (yellow region) (36). The result in *SI Appendix*, Fig. S23*B* indicates that hydrogen gas interacts with this defect site, whereas CO_2 did not show any interactions. The peak between 600 and 700 cm^{-1} [assigned to the absorption of gaseous CO_2 (36)] decreased as the temperature increased, whereas the peak in the 1,050–950-cm^{-1} region that was assigned as bidentatecarbonate (39)continuously increased, indicating that CO_2 was converted into products via a stable bidentate carbonate intermediate (40) (*SI Appendix*, Fig. S23*E*).

As the DRIFT chamber was cooled to room temperature, we were able to trap several intermediate species (*SI Appendix*, Fig. S23*F*). The peaks at 3,135 and 3,032 cm^{-1} were assigned to the C-H stretching of gaseous and adsorbed premethane and methane species (37). The peak at 1,790–1,670 cm^{-1} was also for C-H vibrations (5), while the peaks at 2,260 and 2,240 cm^{-1} were for adsorbed CO_2. The symmetric peaks at 2,180 and 2,095 cm^{-1} correspond to gaseous CO, whereas the peak at 1,903 cm^{-1} corresponds to adsorbed CO (*SI Appendix*, Fig. S23*F*, blue). The peaks corresponding to bridged bidentate carbonate were observed at 1,620–1,670, 1,220–1,270, and 980–1,020 cm^{-1}, whereas those of monodentate carbonate were observed at 1,470–1,530, and 1,300–1,370 cm^{-1} (*SI Appendix*, Fig. S23*F*, gray and light yellow) (39). The sharp peak at 1,397 cm^{-1} was also known to be due to the bidentate bicarbonate (green) (40). Thus, DRIFT study showed various interactions of defect sites with CO_2 and H_2 as well as the formation of reaction intermediates.

Based on the DRIFT, PL, EPR, XPS, PXRD, and catalysis results, the following reaction mechanism is proposed (Fig. 3). CO_2 is first adsorbed on the defect-containing nanosilica by interactions with NBOHC sites and silanols, forming unidentate bicarbonate species (a). At higher temperatures, after hydrogen abstraction, it becomes unidentate carbonate species (b), which is then chemisorbed to nearby oxygen vacancies (ODC) via an oxygen atom (c), which converted into bidentate carbonate species (d). All three species, i.e., unidentate bicarbonate, unidentate carbonate, and bidentate carbonate species were observed in DRIFT study (*SI Appendix*, Fig. S23). The bidentate carbonate species is then converted into a carbon monoxide species by the cleavage of one of C–O bond (e). The first hydrogen molecule is activated by E′ center of species, which then dissociates to form Si-H and preformaldehyde species (f). The preformaldehyde species undergoes surface diffusion to an O vacancy and is chemisorbed via the O atom (g). E′ centers of species (g) dissociate a second molecule of hydrogen and hydrogenate the preformaldehyde species to form formaldehyde species (h). The third molecule of hydrogen is then dissociated by the E′ centers of species (i), converting formaldehyde to premethane species (j). The E′ centers of species (j) then dissociate the fourth molecule of hydrogen to produce methane (l) via transition state (k). Species (l) then loses water molecules to regenerate the O vacancy and E′ centers in defect-containing nanosilica, completing the catalytic cycle and regenerating the catalyst. CO is produced from species (e) without further addition of hydrogen.

In order to get further insight into the proposed mechanistic pathways, we have performed density-functional theory study using the plane-wave technique as implemented in the Vienna Ab Initio Simulation Package (*SI Appendix*, *Computational Details*) (41). Amorphous defect-containing nanosilica surface was modeled considering periodic surface slabs with 14.35 × 7.18-$Å^2$ rectangular surface cell with 53 atoms (Fig. 4*A*). The surface was constructed in such a way that it contains defect sites, namely E′ centers, ODC, and NBOHC as observed in the experimental study. CO_2 adsorbs in a bidentated configuration with carbon atom interacting with NBOHC site on nanosilica surface while one oxygen atom of CO_2 weakly interacts with neighboring Si

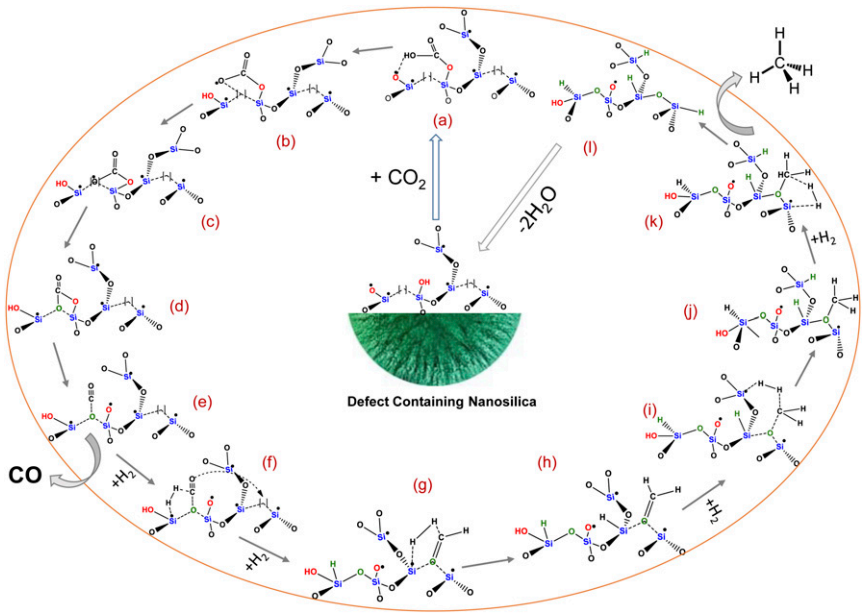

Fig. 3. Schematic of the proposed mechanistic pathway. Here, [ ] indicates O vacancy (ODC center). All defects are shown only in one siloxane network for simplicity, although defects from various other siloxane networks of amorphous silica could also participate in the catalytic cycle. Intermediate species (a–l) are described in the main text.

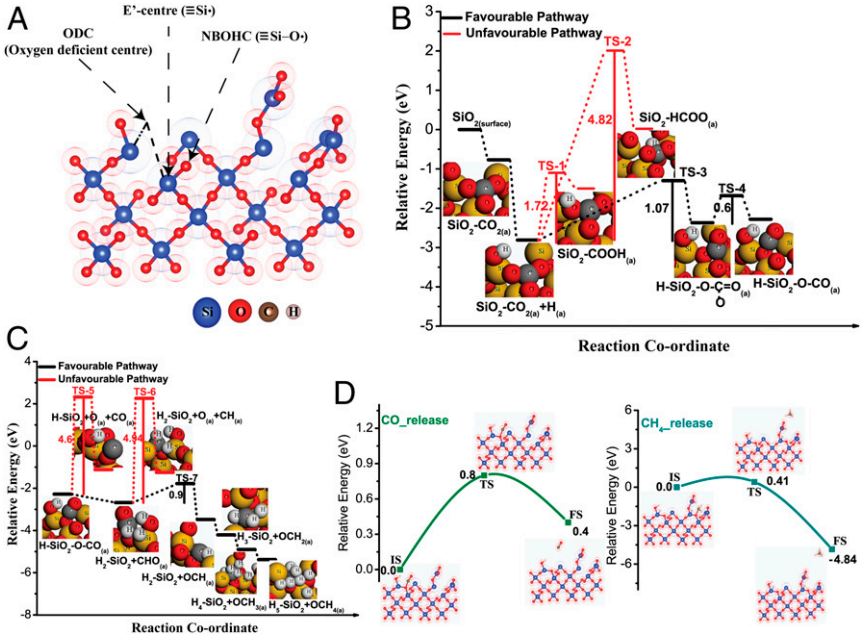

Fig. 4. (*A*) Optimized structure of defect-containing silica surface. (*B*) Potential energy surfaces for CO_2 hydrogenation to CO. (*C*) Potential energy surfaces for methane formation from CO. (*D*) CO and methane release steps from defect-containing silica surface during CO_2 reduction.

center. CO_2 adsorption energy was found to be −0.77 eV with the lengthening of C=O bond in the CO_2 molecule. C–O bond lengths were 1.42 and 1.25 Å, which were higher than the equilibrium bond length of CO_2 (1.16 Å). Bader charge analysis (42, 43) showed a charge transfer of 0.26 e from silica surface to CO_2 indicating activation of CO_2 molecule by defects (44, 45). Charge density difference plot provided further insights about the local charge distribution around the surface and adsorbed CO_2 molecule (*SI Appendix*, Fig. S24). As shown in *SI Appendix*, Fig. S24, there was a negative charge localization on carbon and oxygen atoms of CO_2.

Fig. 4 *B* and *C* shows the relative energy diagram of each elementary step involved in the methane formation via hydrogenation of CO_2 on the defect-containing nanosilica surface. CO formation has been shown in Fig. 4*B*. H-atom adsorption on CO_2-adsorbed surface was thermodynamically favorable. CO_2 reacting with adsorbed H to form either COOH or HCOO were kinetically as well as energetically unfavorable with extremely high activation barriers of 1.72 and 4.82 eV, respectively. On the other hand, the activation barrier for the formation of bidentate carbonate species was relatively low (1.07 eV) and kinetic barrier can be achievable with high-temperature reaction conditions. In the next step, the cleavage of bidentate carbonate species to form adsorbed CO species proceeds through low activation barrier of 0.6 eV. An easy escape of CO from the surface was hindered with an activation barrier of 0.8 eV (Fig. 4*D*). However, this kinetic barrier can be attained by increasing the temperature of the reaction. This finding corroborates with experimental results where the rate of CO formation increases with the increase in reaction temperature.

All of the steps associated with the hydrogenation of CO to CH_4 are energetically favorable with a downhill potential energy profile (Fig. 4*C*). The formation of CHO (the hydrogenation product of CO) was energetically favorable by 0.4 eV whereas the competing CO dissociation step was disfavored by 1.16 eV. The high kinetic barrier (4.6 eV) discarded the possibility of CO dissociation on the silica surface. Although CHO migration to an ODC center of the silica surface was thermodynamically favorable, it was slightly disfavored kinetically with a barrier of 0.9 eV. However, high-temperature reaction conditions can make this process facile by providing sufficient thermal energy. On the contrary, the competing reaction of dissociation of CHO to form surface-adsorbed CH and O was kinetically hindered with an unachievable activation barrier of 4.94 eV. Therefore, reaction proceeded via CHO migration to form OCH species and subsequent hydrogenation of OCH occurred giving rise to OCH_2 (Fig. 3). The hydrogenation of OCH_2, followed by OCH_3 was energetically highly favorable to produce adsorbed OCH_4 species. Finally, CH_4 was released from the surface with a small activation barrier of merely 0.41 eV, which was facile at the reaction temperature used during catalysis. From the above detailed mechanistic study (experiment and theory), it can be concluded that CO_2 reduction to form CH_4 catalyzed by defects in nanosilica is favorable, thermodynamically and kinetically.

Conclusion

Defect-containing nanosilica was found to be an alternative catalyst to expensive noble metals as well as complex organometallic-based catalysts. In this work, we observed that by generating and tuning the defects (type, concentration, and proximity) in nanosilica, CO_2 can be transformed into green fuel (methane) with good productivity and selectivity without the use of any metal nanoparticles. The optimum concentration of E′ centers, ODC, and NBOHC defect sites were needed, which allowed the defects to work synergistically to activate CO_2 and dissociate hydrogen, thus converting CO_2 to methane.

Unlike metal catalysts, whose activity decreases significantly with time, the loss of activity in the defect-containing silica catalysts was less significant. Notably, the regeneration of the defect-containing silica only required air (rather than hydrogen gas required for metal catalysts). Surprisingly, the catalytic activity of DNS-25 for methane production increased significantly after every regeneration cycle, reaching more than double the methane production rate (9,569 μmol $g^{-1}{\cdot}h^{-1}$) after eight regeneration cycles as compared to the initial catalyst performance (3,810 μmol $g^{-1}{\cdot}h^{-1}$). Also, defect-containing silica DNS-25 showed 6.6× more activity as compared to parent DFNS material, indicating the good potential of our defect-engineering approach. This activated catalyst remained

stable for more than 200 h with a good formation rate and selectivity.

Thus, this magnesiothermic defect-engineering protocol may allow the development of metal-free nanocatalysts for CO_2 conversion at the significant rates, scales, and stabilities required to make the process economically competitive. This metal-free approach could also have a multidisciplinary impact and may facilitate the rational design of catalysts for various other catalytic processes apart from CO_2 conversion.

Experimental Methods

Synthesis of Defect-Containing Nanosilica Using the Magnesiothermic Protocol. In a typical synthesis, 250 mg DFNS and 10, 25, and 50 wt % Mg powder was mixed well with a mortar and pestle. The whitish-gray powder was then transferred to a tubular quartz tube, which was degassed overnight to remove atmospheric oxygen. The tube was then sealed under vacuum and heated in a furnace to 675 °C at a rate of 5 °C min^{-1} and then held at this temperature for 12 h. The gray powder (defect-containing nanosilica and MgO) was collected by breaking the tube. The samples were then stirred with an acidic solution (6.8 mL HCl 12 M, 17 mL H_2O, and 52 mL ethanol) for 24 h at room temperature to dissolve the MgO. The solid product was isolated by centrifugation. This step was repeated three times, and after that samples were washed by 40 mL each of water and ethanol twice. Washing was continued until all Mg-containing species such as Mg_2SiO_4, MgO, and Mg were completely absent from the defect-containing silica, which was monitored by EDS elemental analysis, and their absence was further confirmed by PXRD and XPS. The samples were dried in an oven overnight and the defect-containing nanosilica powder was stored under atmospheric conditions.

Characterization. Scanning TEM analysis was carried out on FEI-TITAN operated at an accelerating voltage of 300 kV. The samples were prepared by dispersing a small amount of powder in ethanol by sonication and dropping the solution on a 200-mesh carbon-coated TEM grid. Elemental analysis was achieved using the energy-dispersive X-ray spectroscopy (EDS). A Panalytical X'Pert Pro powder X-ray diffractometer was used to record X-ray diffraction patterns using a Cu $K\alpha$ source. The surface area, pore-volume, and pore-size distribution measurements were carried out using Micromeritics Flex-3 analyzer by applying BET theory to the N_2 physisorption data. Before analysis, all samples were degassed at 120 °C for 12 h. A UV/vis/near-infrared spectrophotometer was used to record the UV-DRS of all samples. The Fourier transform infrared (IR) spectra were recorded using JASCO FT/IR-4700. The EPR spectra of all samples were recorded at room temperature using a JEOL EPR spectrometer. The following conditions were used to record EPR spectra of the catalyst: amount = 30 mg, power = 5 mW, modulation frequency =100 kHz, number of scans = 5. XPS measurements were carried out using a Thermo $K\alpha+$ spectrometer using microfocused and monochromated Al-K_α radiation with an energy of 1486.6 eV. Charge correction of all spectra was achieved by fixing the energy of the C1s peak at 284.5 eV. All fitting was done in XPSPEAK 4.1 by taking Taugaard background. For the PL measurements, excitation was carried out at 374 nm using a diode laser, with the sample placed in the integrating sphere. For the DRIFT study, the IR spectra were recorded using a mixture of 3.5 mg catalyst and 156 mg KBr powder in a closed reactor chamber, with a heater and gas-flow controller. The catalyst was activated at 550 °C with 50 mL min^{-1} air before the measurements. After cooling to the desired temperature, the feed gases (2.5 mL CO_2 and 10 mL H_2) were passed through the chamber, and IR spectra were recorded over time under different reaction conditions.

Catalytic CO_2 Conversion. The methanation reaction was carried out in a fixed-bed continuous-flow reactor (PIDengtech). Into a tubular reactor of diameter 0.9 cm and length 12 cm, 200 mg of catalyst was placed. The reactor was heated to 550 °C at a rate of 20 °C min^{-1} with 50 mL min^{-1} flow of air to remove atmospheric carbon contamination. After cooling the reactor to 400 °C in the presence of air and N_2, the reactive gases were fed (2.5 mL min^{-1} CO_2, 10 mL min^{-1} H_2 and 2.5 mL min^{-1} N_2 as an internal standard) by mass-flow controllers for individual gases. The reaction progress and product quantification was achieved by gas chromatography (Agilent 7890 B) with a flame ionization detector and thermal conductivity detector using an Agilent hybrid column CP7430 to separate the CO_2, CH_4, and CO. Peltier cooling was used to condense and collect the water by-product from the reactor.

Data Availability. The data presented in this article are available in *SI Appendix*. *SI Appendix* contains more experimental and computational details, SAED, PXRD, EPR, PL, UV-DRS, DRIFT, XPS, Auger spectra, additional catalysis data and reaction progress plots with time, Raman data, TGA, and computational details.

ACKNOWLEDGMENTS. This work was supported by the Department of Atomic Energy, Government of India. We acknowledge the electron microscopy and XRD facilities of Tata Institute of Fundamental Research (TIFR), Mumbai. We thank Prof. Ranjan Das and Prof. Sandip Ghosh (TIFR, Mumbai), Dr. Vinod Prabhakaran (National Chemical Laboratory, Pune), Prof. Jan Valenta (Charles University), and Dr. Vinayak Rane (Bhabha Atomic Research Centre, Mumbai) for EPR, preliminary PL, XPS, PL, and EPR, respectively. We also thank Prof. R. Venkataramani, Prof. J. Dasgupta, and Mr. Ayan Maity (TIFR, Mumbai) for critical discussions on this work. A.D. thanks the Science and Engineering Research Board (SERB) and Department of Science and Technology (DST) for computational resources from extramural research grants.

1. A. Kätelhön, R. Meys, S. Deutz, S. Suh, A. Bardow, Climate change mitigation potential of carbon capture and utilization in the chemical industry. *Proc. Natl. Acad. Sci. U.S.A.* **116**, 11187–11194 (2019).
2. J. Jia *et al.*, Heterogeneous catalytic hydrogenation of CO_2 by metal oxides: Defect engineering–Perfecting imperfection. *Chem. Soc. Rev.* **46**, 4631–4644 (2017).
3. S. Rönsch *et al.*, Review on methanation–From fundamentals to current projects. *Fuel* **166**, 276–296 (2016).
4. C. Vogt *et al.*, Unravelling structure sensitivity in CO_2 hydrogenation over nickel. *Nat. Catal.* **1**, 127–134 (2018).
5. W. Sun *et al.*, Heterogeneous reduction of carbon dioxide by hydride-terminated silicon nanocrystals. *Nat. Commun.* **7**, 12553 (2016).
6. P. G. O'Brien *et al.*, Photomethanation of gaseous CO_2 over Ru/Silicon nanowire catalysts with visible and near-infrared photons. *Adv. Sci. (Weinh.)* **1**, 1400001 (2014).
7. C. Qian *et al.*, Catalytic CO_2 reduction by palladium-decorated silicon–hydride nanosheets. *Nat. Catal.* **2**, 46–54 (2018).
8. J. Yang *et al.*, Single atomic vacancy catalysis. *ACS Nano* **13**, 9958–9964 (2019).
9. B. M. Ceballos, J. Y. Yang, Directing the reactivity of metal hydrides for selective CO_2 reduction. *Proc. Natl. Acad. Sci. U.S.A.* **115**, 12686–12691 (2018).
10. Y. Wang *et al.*, CO_2 reduction to acetate in mixtures of ultrasmall (Cu)n,(Ag)m bimetallic nanoparticles. *Proc. Natl. Acad. Sci. U.S.A.* **115**, 278–283 (2018).
11. Z. He *et al.*, Synthesis of liquid fuel via direct hydrogenation of CO_2. *Proc. Natl. Acad. Sci. U.S.A.* **116**, 12654–12659 (2019).
12. T. N. Huan *et al.*, Low-cost high-efficiency system for solar-driven conversion of CO_2 to hydrocarbons. *Proc. Natl. Acad. Sci. U.S.A.* **116**, 9735–9740 (2019).
13. N. G. Patil *et al.*, Carboxylate salts as ideal initiators for the metal-free copolymerization of CO_2 with epoxides: Synthesis of well-defined polycarbonates diols and polyols. *Macromolecules* **52**, 2431–2438 (2019).
14. J. Hong, C. Jin, J. Yuan, Z. Zhang, Atomic defects in two-dimensional materials: From single-atom spectroscopy to functionalities in opto-/electronics, nanomagnetism, and catalysis. *Adv. Mater.* **29**, 1606434 (2017).
15. C. T. Campbell, C. H. F. Peden, Oxygen vacancies and catalysis on ceria surfaces. *Science* **309**, 713–714 (2005).
16. R. J. D. Tilley, "Defects in solids" in *Encyclopedia of Inorganic Chemistry*, R. A. Scott, Ed. (John Wiley & Sons, Ltd., 2008), pp. 1–513.
17. G. Ou *et al.*, Tuning defects in oxides at room temperature by lithium reduction. *Nat. Commun.* **9**, 1302 (2018).
18. J. Jupille, G. Thornton, *Defects at Oxide Surfaces* (Springer, 2015).
19. M. Y. S. Hamid *et al.*, Oxygen vacancy-rich mesoporous silica KCC-1 for CO_2 methanation. *Appl. Catal. A Gen.* **532**, 86–94 (2016).
20. V. Zeleňák, A. Zeleňáková, J. Kováč, Insight into surface heterogeneity of SBA-15 silica: Oxygen related defects and magnetic properties. *Colloids Surf. A Physicochem. Eng. Asp.* **357**, 97–104 (2010).
21. Y. D. Glinka, S. H. Lin, L. P. Hwang, Y. T. Chen, Photoluminescence from mesoporous silica: Similarity of properties to porous silicon. *Appl. Phys. Lett.* **77**, 3968–3970 (2000).
22. S. Banerjee, S. Maity, A. Datta, Enhanced trapping efficiency in acid-treated silica nanostructures. *J. Phys. Chem. C* **115**, 22804–22809 (2011).
23. V. Polshettiwar, D. Cha, X. Zhang, J. M. Basset, High-surface-area silica nanospheres (KCC-1) with a fibrous morphology. *Angew. Chem. Int. Ed. Engl.* **49**, 9652–9656 (2010).
24. A. Maity, R. Belgamwar, V. Polshettiwar, Facile synthesis to tune size, textural properties and fiber density of dendritic fibrous nanosilica for applications in catalysis and CO_2 capture. *Nat. Protoc.* **14**, 2177–2204 (2019).
25. Z. Bao *et al.*, Chemical reduction of three-dimensional silica micro-assemblies into microporous silicon replicas. *Nature* **446**, 172–175 (2007).
26. J. R. Wynnyckyj, D. B. Rao, The mechanism of reduction of silica by magnesium vapor. *High Temp. Sci.* **8**, 203–217 (1976).
27. L. Skuja, Section 1. Defect studies in vitreous silica and related materials: Optically active oxygen-deficiency-related centers in amorphous silicon dioxide. *J. Non-Cryst. Solids* **239**, 16–48 (1998).
28. A. Colder *et al.*, Strong visible photoluminescence from hollow silica nanoparticles. *Nanotechnology* **15**, L1–L4 (2004).

29. A. N. Trukhin, H. J. Fitting, T. Barfels, A. Von Czarnowski, Cathodoluminescence and IR absorption of oxygen deficient silica–Influence of hydrogen treatment. *J. Non-Cryst. Solids* **260**, 132–140 (1999).
30. M. R. Shaneyfelt, P. S. Winokur, D. M. Fleetwood, J. R. Schwank, W. L. Warren, Hydrogen interactions with delocalized spin centers in buried SiO_2 thin films. *Appl. Phys. Lett.* **62**, 1661–1663 (2002).
31. T. V. Larina *et al*., Influence of the surface layer of hydrated silicon on the stabilization of Co^{2+} cations in Zr–Si fiberglass materials according to XPS, UV-Vis DRS, and differential dissolution phase analysis. *RSC Adv.* **5**, 79898–79905 (2015).
32. B. Tesson *et al*., Surface chemical composition of diatoms. *ChemBioChem* **10**, 2011–2024 (2009).
33. C. Fernández-Sánchez, J. A. Rodríguez, C. Domínguez, Synthesis of sol–gel SiO_2-based materials using alkoxydisilane precursors: Mechanisms and luminescence studies. *J. Sol-Gel Sci. Technol.* **73**, 417–427 (2014).
34. H. Aguiar, J. Serra, P. González, B. León, Structural study of sol-gel silicate glasses by IR and Raman spectroscopies. *J. Non-Cryst. Solids* **355**, 475–480 (2009).
35. L. X. Yi, J. Heitmann, R. Scholz, M. Zacharias, Phase separation of thin SiO layers in amorphous SiO/SiO_2 superlattices during annealing. *J. Phys. Condens. Matter* **15**, S2887–S2895 (2003).
36. D. E. Vázquez-Valerdi *et al*., Compositional and optical properties of SiOx films and (SiOx /SiOy) junctions deposited by HFCVD. *Nanoscale Res. Lett.* **9**, 422 (2014).
37. J. Coates, "Interpretation of infrared spectra, a practical approach" in *Encyclopedia of Analytical Chemistry*, R. A. Meyers, Ed. (John Wiley & Sons, 2000), pp. 10815–10837
38. A. Ueno, C. O. Bennett, Infrared study of CO_2 adsorption on SiO_2. *J. Catal.* **54**, 31–41 (1978).
39. H. Li *et al*., Synthesis of glycerol carbonate by direct carbonylation of glycerol with CO_2 over solid catalysts derived from Zn/Al/La and Zn/Al/La/M (M = Li, Mg and Zr) hydrotalcites. *Catal. Sci. Technol.* **5**, 989–1005 (2015).
40. E. M. Köck, M. Kogler, T. Bielz, B. Klötzer, S. Penner, In situ FT-IR spectroscopic study of CO_2 and CO adsorption on Y_2O_3, ZrO_2, and Yttria-stabilized ZrO_2. *J. Phys. Chem. C Nanomater Interfaces* **117**, 17666–17673 (2013).
41. G. Kresse, J. Hafner, Ab initio molecular dynamics for liquid metals. *Phys. Rev. B Condens. Matter* **47**, 558–561 (1993).
42. G. Henkelman, A. Arnaldsson, H. Jónsson, A fast and robust algorithm for Bader decomposition of charge density. *Comput. Mater. Sci.* **36**, 354–360 (2006).
43. R. F. W. Bader, *Atoms in Molecules: A Quantum Theory* (Oxford University Press, Oxford, 1990).
44. M. Zhang, M. Dou, Y. Yu, DFT study of CO_2 conversion on $InZr_3$(110) surface. *Phys. Chem. Chem. Phys.* **19**, 28917–28927 (2017).
45. A. K. Mishra, A. Roldan, N. H. Leeuw, CuO surfaces and CO_2 activation: A dispersion-corrected DFT+U study. *J. Phys. Chem. C* **120**, 2198–2214 (2016).